

Rationally Designed Anti-Glare Panel Arrays as Highway Wind Energy Harvester

Erming Su, Hao Li, Jiabin Zhang, Zijie Xu, Baodong Chen, Leo N.Y. Cao,*
and Zhong Lin Wang*

The anti-glare panels along highways can block the dazzling lights of opposing vehicles at night, playing an important role in the highway safety. Inspired by the highway anti-glare panels, wind energy harvesting triboelectric nanogenerator (AG-TENG) arrays to properly capture energy from highway moving vehicles is developed. A single AG-TENG installation module can achieve a high power density of 0.2 W m^{-2} at a wind speed of 3 m s^{-1} . This wind speed is too low to drive conventional wind energy harvesting equipment. The performance of the AG-TENG shows no degradation after 80 h of continuous operation (1 440 000 times). Thus, with the rational consideration and features, the system can generate enough power to drive internet of things (IoT) devices and environmental sensors, as well as offer wireless alarming and radio frequency identification vehicle monitoring. This study provides a promising strategy to properly harvest wind energy on highways using existing infrastructures under the condition of even no natural wind, showing broad application prospects in distributed environmental monitoring, intelligent highways, and the IoT.

1. Introduction

In recent years, due to the continuous growth of the world population and total energy consumption, traditional fossil energy, and coal-based low-entropy energy will not be able to meet human's long-term demand for energy, leading to a conflict between growing energy demands and limited supply of energy for many countries. Therefore, the use of renewable distributed energy sources such as wind, solar, and water wave to generate electricity has received worldwide attention.^[1] Among the various energies, the wind energy on the highway (which is widespread around the world) draws attention due to its constant direction and continuous output, compared with the randomness of other natural energies. In fact, studies have found that high-speed vehicles will cause strong disturbances to the air on the highway as wind energy.^[2]

The idea of harvesting energy from vehicle wakes was proposed for a long time^[3] and many patents have also been filed.^[4] Depending on the speed and size of the moving vehicle, the generated wind speed may reach 24 m s^{-1} , capable of hitting the wind turbine blades at speeds of up to 6 m s^{-1} .^[5] Therefore, this is a feasible way to reuse some of the constants but wasted energy. In addition to the experimental observations, many studies have modeled the wake flow of moving vehicles,^[6] providing a great reference for further evaluating and optimizing the turbine performance. However, it is still challenging to develop suitable devices for highway wind energy harvesting.

The triboelectric nanogenerator (TENG), invented by Wang's group in 2012, is a great candidate for sustainable random wind energy harvesting.^[7] TENG is mainly a device that can convert random mechanical energy in the environment, including wind energy,^[8] ocean energy,^[9] and human movement,^[10] into electrical energy by coupling contact electrification^[11] and electrostatic induction.^[12] In addition, TENG can also be designed as various battery-free sensors for sensing, such as vibration monitoring,^[12d,13] tactile sensing,^[14] angle detection,^[15] and fluid monitoring.^[16] Further integration with EMG can provide a promising strategy for green energy harvesting.

Many studies are using TENG to harvest wind energy in the transportation field. For example, Zhang et al. designed a


E. Su, H. Li, J. Zhang, Z. Xu, B. Chen, L. N.Y. Cao, Z. L. Wang
CAS Center for Excellence in Nanoscience
Beijing Key Laboratory of Micro-nano Energy and Sensor
Beijing Institute of Nanoenergy and Nanosystems
Chinese Academy of Sciences
Beijing 101400, P. R. China
E-mail: caonanying@binn.cas.cn

E. Su, H. Li, J. Zhang
Center on Nanoenergy Research
School of Physical Science and Technology
Guangxi University
Nanning 530004, P. R. China

Z. Xu
School of Nanoscience and Technology
University of Chinese Academy of Sciences
Beijing 100049, P. R. China

B. Chen
Institute of Applied Nanotechnology
Jiaxing, Zhejiang 314031, P. R. China

Z. L. Wang
Georgia Institute of Technology
Atlanta, GA 30332-0245, USA
E-mail: zhong.wang@mse.gatech.edu

 The ORCID identification number(s) for the author(s) of this article can be found under <https://doi.org/10.1002/adfm.202214934>.

DOI: 10.1002/adfm.202214934

hybrid electromagnetic-triboelectric nanogenerator based on a spinning disk,^[16a] which can be used to harvest airflow energy generated by a car moving inside a tunnel. Furthermore, Bian et al. designed a biomimetic triboelectric nano-bionic tree composed of leaf cells and stem cells,^[17] to harvest natural and motion-induced wind energy for subway tunnel lighting, but the work is limited by the high wind speed required ($\approx 11 \text{ m s}^{-1}$). Recently, Zhang et al. introduced an elastic contact structure design in a rotating TENG,^[18] demonstrating its potential application in smart high-speed trains. However, this structure has some degree of wear and tear, causing the output reduction after long-term operation (80% after 250 000 tests). Therefore, it is still a great challenge to improve the output performance, durability, and wear resistance of TENGs during long-term operation.^[19]

Most importantly, an effective device, not to mention a robust network, for harnessing wind energy along highways has not yet been developed. In addition, adding a huge generator network to the highway infrastructure without careful consideration and planning is impractical, and could be troublesome and hazardous. For example, the wind turbines designed by Kim et al. to be installed above the highway may have collision and safety hazards.^[20] Fortunately, many highways start to densely place lots of anti-glare panels ($\approx 50 \text{ cm}$ as intervals) in the median of two-direction highways to avoid light-related traffic accidents by blocking the strong light from oncoming traffic. This gives us inspiration and opportunities to invent energy-harvesting devices and systems functioning as anti-glare panels, while also harvesting energy.

Therefore, in this study, we propose a proper large-scale system to harvest wind energy on highways with modular soft-contact AG-TENG devices in network. The device applied

ternary electrodes^[21] to maximize the output and force-balance spacing feature^[22] to maintain optimal distance between triboelectric layers to reduce potential friction and wear. Unlike previous work, our system, which can replace the traditional anti-glare panels, will not introduce extra safety issues to the highway infrastructure. More importantly, compared with traditional, fixed anti-glare panels, this AG-TENG used a rotational vortex turbine with aerodynamic design that drastically reduces the device drag force from the wind and improves the system's durability. As a result, the system's durability can further reduce the risk of device breaking and thus the highway hazard.

By continuously optimizing the structural parameters of the system, the TENG's performance was improved. Experiments show that it can achieve a high average power density of 0.2 W m^{-2} . In addition, the device shows no materials degradation, and output decrease after 80 h of continuous operation (1440 000 times). Finally, combined with a power management system, the system can harvest breeze energy (3 m s^{-1}) to drive the internet of things (IoT) devices, such as humidity thermometers, wireless alarms, and the radio frequency identification (RFID) system for vehicle identification and monitoring, providing a promising strategy for smarter and safer highways.

2. Results and Discussion

2.1. Structure and Working Principle of the AG-TENG Device

The AG-TENG system can block the strong light from traffic in opposite directions while harvesting the wind energy generated by oncoming vehicles on the highway. As shown in Figure 1a, we can install it in the road median every certain

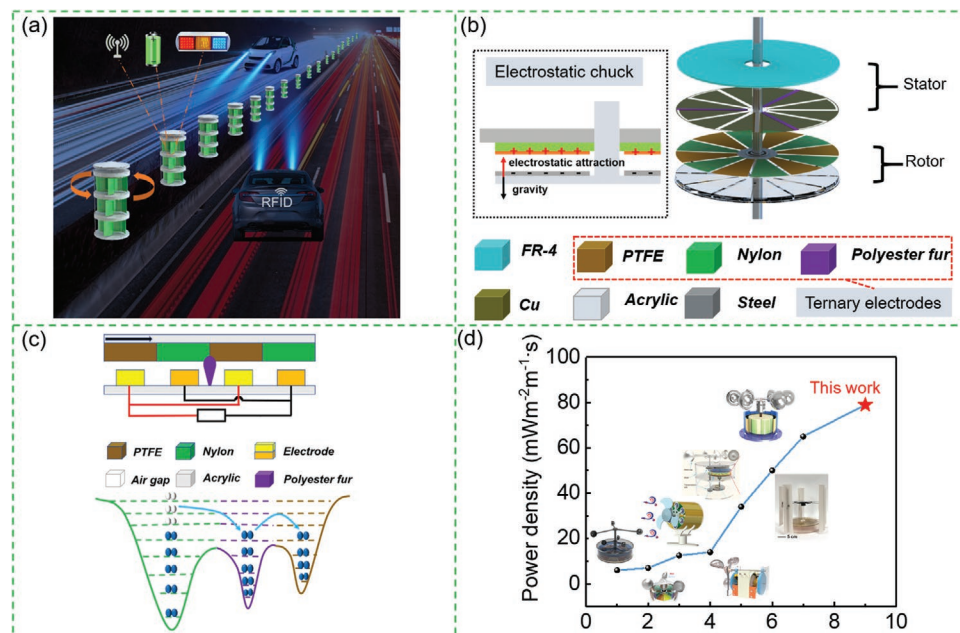


Figure 1. Structural design and working mechanism of AG-TENG. a) The configuration of AG-TENGs installed in the highway isolation belt every other section. b) Schematic diagram of the structure of AG-TENG. c) Schematic crosssection of the AG-TENG and the electron cloud potential well model of the surface charge transfer in the contact state for the three dielectric materials. d) Comparison of the peak power density per unit wind speed of the AG-TENG with other related devices.

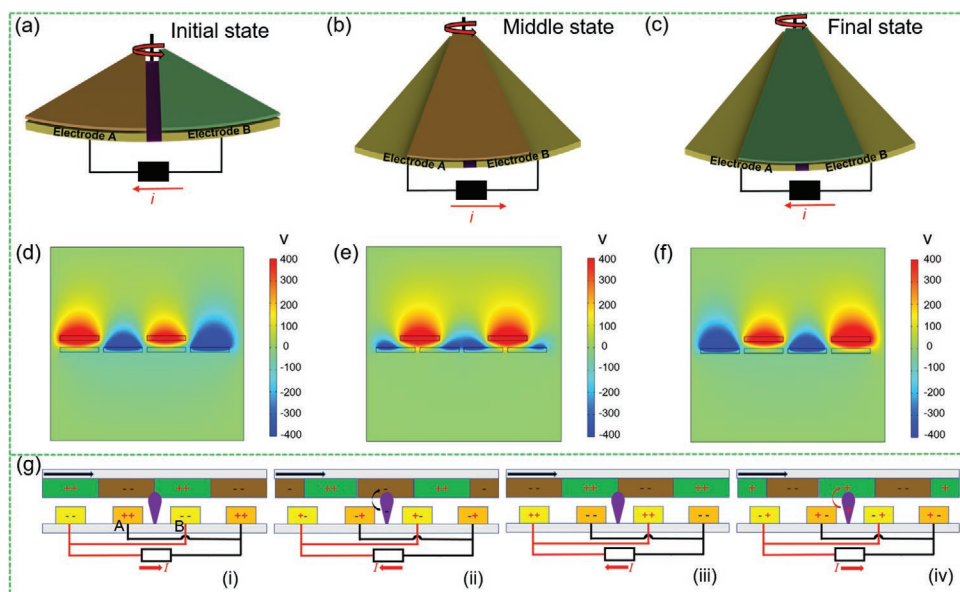


Figure 2. Schematic diagram of the working principle of AG-TENG. a–c) Schematic diagram of the operating state of the quarter-cycle of AG-TENG: initial state a), middle state b) and final state c). d–f) Schematic diagram of the potential distribution of COMSOL simulation in the open circuit state. g) Schematic diagram of current and charge distribution in the short-circuit state.

distance according to the light blocking requirement. Therefore, the constant wind generated by the traffic flow can be harvested by the AG-TENG system to realize close-looped self-powered sensing and identification for the smart and efficient highway.

The TENG device used ternary dielectric triboelectrification to achieve high output.^[21] The ternary dielectric structure is shown in Figure 1b and Figure S1 (Supporting Information), which is mainly composed of rotor and stator. The rotor surface is alternately affixed with polytetrafluoroethylene (PTFE) film and nylon (PA) film as dielectric layer; the stator adopts copper foil (4 mm gap to avoid electrical breakdown) on the surface of PCB circuit board as the induction electrode with three polyester furs as the ternary dielectric layer. The working mechanism of this ternary structure will be introduced later. This ternary structure has the following advantages: 1) increasing the rotor area, from 50% (for normal sliding TENG) to 100% to drastically increase output, 2) allowing materials of opposite polarity to transfer electrons, but do not directly contact to reduce system wear, increasing material selectivity. The detailed fabrication process of AG-TENG can be found in the experimental section.

To better explain the triboelectric design of the ternary structure, we presented a model diagram of the electron cloud barrier in Figure 1c to illustrate the surface electron transfer in contact between the three dielectric materials. Figure 1c shows that when atoms of nylon material and atoms of polyester fur material approach and contact respectively, the electron clouds overlap, forming an asymmetric double-well potential. Due to the overlap of strong electron clouds, the energy barrier between the two is reduced so that the electron can hop from the atom of nylon (higher energy level) to the atom of polyester fur (lower energy level), generating contact electrification. The same process occurs from the atoms of polyester fur and PTFE

atoms. In Figure S2 (Supporting Information), the scanning electron microscope (SEM) images of the surfaces of PTFE and nylon membranes before and after use shows minimum surface wear. Therefore, in order to better evaluate the output performance of TENG, normalized power density measurements under different wind speeds are used to compare with previous work, as shown in Figure 1d. The power density per unit wind speed of AG-TENG is $79 \text{ mWm}^{-2} \text{ m}^{-1} \text{ s}$, which is significantly better than the previous work.^[19b,22,23]

Here, we describe the charge transfer mechanism in detail (Figure 2). For the convenience of explanation, we defined three contact states. Figure 2a–c shows a schematic diagram of the operating state of the AG-TENG quarter cycle. When the rotor rotates, the polyester fur contacts the PTFE membrane (Figure 2a, the initial state). Since the electronegativity of PTFE is higher than that of polyester fur, the contact and separation between them will lead to the separation of positive and negative charges (Figure 2b, the middle state). As the rotor turns, the polyester fur touches the nylon film, and electrons from the nylon film transfer to the polyester fur. At the same time, the contact between the nylon film and the polyester fur will generate triboelectric charges, so that more electrons are injected into the polyester fur, until the next piece of PTFE and the polyester fur touch and rub again, which brings more electrons to the PTFE (Figure 2c, final state). If sliding continues, the external load redistributes the charge on the electrodes to balance the potential difference. Such cyclical electric induction can ensure the continuous AC output of AG-TENG. This will greatly improve the voltage output of AG-TENG. Finite element simulation using COMSOL was conducted to replicate this cyclical induction process in Figure 2d–f. The distribution of the electric potential also confirms the direction of charge transfer between polyester fur and PTFE.

The schematic explanation of the entire process to generate current is shown in Figure 2g. When the polyester fur is transferred from the starter state i) to PTFE, electrons flow from the B electrode to the external circuit to equalize the potential difference. The resulting induced current flows from electrode A to electrode B ii) until it leaves the PTFE. As the polyester skin is further transferred to the nylon film, electrons flow from electrode A to the external circuit, generating an induced current iii). As the rotor continues to rotate, the periodic charge transfer between electrodes A and B will produce an alternating current iv), providing power to the external load. After a certain period of cycle test, the surface charges of PTFE and nylon gradually reach saturation.

2.2. Optimization of Structural Device Parameters

To ensure the stable operation of the generator unit in the highway environment, we optimized the performance in the laboratory by fine-tuning the clearance and resistance. The standardized test platform for this experiment is shown in Figure 3a. The AG-TENG device is fixed on the horizontal XY-direction platform, whose accuracy can reach 0.1 mm. Meanwhile, the fine-tuning rotating handle ensures the absolute distance between the rotor and the stator.

To reveal the effect of rotational speed on the output performance, we measured the short-circuit current (Isc),

open-circuit voltage (Voc), and transferred charge (Qsc) of the 12-grid 3-stripe polyester fur with PA and PTFE, as shown in Figure 3b–d, as the motor speed changes from 100 to 800 rpm, the current gradually increases, from 5 to 60 μA , because the higher the speed, the higher the frequency of rub between the two, which increases the current. However, the voltage and charge, not affected by frequency, stabilized at ≈ 2.4 kV and 295 nC, respectively.

In addition, we also investigated the charging performance of the device, as shown in Figure 3e. The 100 μF capacitor can be charged to 10 V in only two minutes. Subsequently, we tested the peak output power and average power of the device (Figure 3f; Figure S3a, Supporting Information). The formula for calculating peak output power is:

$$P = I(t)^2 R \quad (1)$$

In the formula, R is the load resistance, and I(t) is the instantaneous current through the resistance. The average power of TENG can be calculated by the following formula:

$$P_{\text{ave}} = \frac{\int_0^T I(t)^2 R dt}{T} \quad (2)$$

I(t) is the current flowing through the resistor at time t, R is the resistance, and t is the integration time. When the matching resistance is 100 M Ω , the peak power reaches the maximum

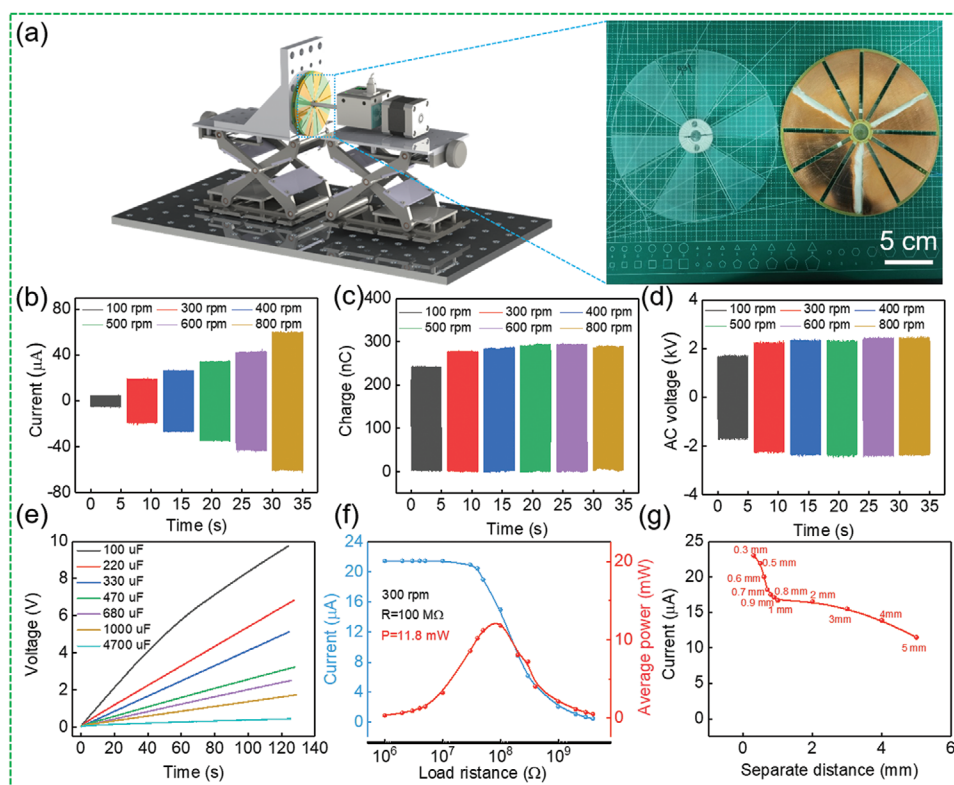


Figure 3. AG-TENG performance optimization. a) Schematic diagram of the dynamic torque measurement system for AG-TENG performance optimization. The inset is a photo of the rotor and stator. Output performance at different speeds b) short circuit current, c) output charge, d) open circuit voltage. e) Characteristic curves of charging capacitors with different capacities at 300 rpm. f) AG-TENG peak output power characteristic curve. g) Current output characteristics under different gaps.

value of 22 mW and the average power reaches 11.8 mW. The detailed calculation process of average power is shown in the notes in Note S1 (Supporting Information). Furthermore, similar to the conventional TENG, the output of the AG-TENG increases with the increase of torque (Figure S3b, Supporting Information).

Since the electrostatic induction is highly affected by the electrical field and the distance, therefore the gap has a crucial impact on the output effect of the current. As shown in Figure 3g and Figure S3d (Supporting Information), as the gap between the rotor and the stator gradually decreases, the output current between the two will gradually increase. However, due to the limitations of the experimental equipment, the stability of the rotor at high speed is not very satisfactory, and 0.3 mm is the shortest separation distance (rotation speed: 300 rpm) that can be achieved in this work. During the experiment, in order to ensure the integrity of the device and the stability of the experimental results, we used the optimal setting with a gap of 0.5 mm for the experiment.

The effects of device structure and material on the output performance of AG-TENG were also investigated. First in order to reveal the influence of the number of grids on the output effect, we carried out tests with 4, 6, 8, and 12 grids respectively, as shown in Figure S4a–c (Supporting Information), when the experimental speed set to 300 rpm, it was finally found that as the number of grids increased, the current increased from 7.23 μA at the beginning to 20.23 μA . The voltage remains basically the same and the charge increases by ≈ 12 nC. This shows that when the contact area is fixed, the output current is proportional to the number of grids. This is mainly because when the number of grids increases, the frequency of contact separation between triboelectric materials will increase correspondingly, which will lead to an increase in charge transfer rate and thus increase the current.

Second, to explore the output effect of the best material, we also replaced the rotor with different electronegative triboelectric materials. The experimental results are shown in Figure S4d,e (Supporting Information) (800 rpm). The results show that when the positive electrode material in the rotor is PA when the film anode material is PTFE film, the output effect reaches the maximum value. In addition, whether the triboelectric material on the stator is trimmed or not has a significant impact on the output. As shown in Figure S5 (Supporting Information), polyester fur showed the best output effect during the test, because the polyester fur electropositivity is worse than that of rabbit hair, which ensures that it will generate more charge transfer during the rub process with PA and PTFE.

2.3. Device Performance under Fan Conditions

To verify the feasibility of AG-TENG for wind energy collection, a blower was used as the wind source to conduct performance characterization. Figure 4a–c show the output performance (short circuit current, open circuit voltage, and transferred charges) of a single TENG device at different wind speeds. The adjustable wind speed range of the fan is 0–7 m s^{-1} . As shown in Figure 4a, the current increases gradually with the increase

of wind speed, and the current reaches 20 μA when the wind speed at 7 m s^{-1} , the voltage does not change much. Because the increase of wind speed will shorten the time of each charge transfer cycle when the transfer charge is saturated, but the area of contact didn't change at all.

Besides the regular performance, we demonstrated the capacitor charging capability of the AG-TENG device in Figure 4d,e. Figure 4d shows the charging voltage curve of the device under the wind speed of 3 m s^{-1} for capacitors with different capacities. It can be seen that for different capacitors of 100–4700 μF , the voltage can reach 5.9–1.2 V respectively within 120 s. Figure 4e shows the charging voltage curve of the 1000 μF capacitor under different wind speeds. The wind speed setting gradient is from 3 to 7 m s^{-1} , and the charging speed also increases with the increase of the wind speed. Figure 4f shows the comparative changes of TENG output performance under different wind speeds. In addition, we also studied the relationship between the output power and resistance of the device at a wind speed of 3 m s^{-1} , as shown in Figure 4g and Figure S3c (Supporting Information). The instantaneous peak power of a single device reaches a maximum value of 4 mW and the average power reaches 2.2 mW at the matching resistance of 100 $\text{M}\Omega$. The output power per unit wind speed (4 mW m s^{-1}) is 12.2 times, compared with the similar work.^[17]

In addition, we explored the relationship between the rotor and the stator and between different triboelectric materials and the TENG output. Here, several common material combinations are selected: PA/PTFE and copper, PA and rabbit fur, PTFE and rabbit fur, PA/PTFE and rabbit fur, and PA/PTFE and polyester fur. It can be seen from Figure 4h that PA/PTFE and polyester fur have a good electrification effect. However, considering that the rabbit hair material is easily restricted by the environment and is not suitable for mass industrial production, the final Polyester fur for easy industrial production was chosen. Furthermore, we present the durability test results of AG-TENG-TENG in Figure 4i, the output of the device did not decrease after 1440000 cycles of continuous testing for 80 h. In addition, the output performance and characteristics of the AG-TENG and the previous representative hybrid generators are compared in Table S1 (Supporting Information). AG-TENG can efficiently harvest wind energy at low wind speeds. The detailed calculation method can be found in Note S3 (Supporting Information).

2.4. Application of AG-TENG Device

The AG-TENG system is different from the traditional rotary TENGs. The modular structural design as shown in Figure 5a can achieve the effect of high-efficiency collection of wind energy and anti-glare function. In general rotary disc TENG with soft-contact mode, the rotor is above the stator, leaving some shortcomings in the design. For example, the electrostatic attraction and gravity will bring the rotor closer to the stator and warp the rotor over time, and eventually increase the friction and wear, and reduce the overall performance and output. To tackle the issue of gradually reduced gap and warping, the rotor was designed below the stator, using gravity of the rotor to counter the attractive electromechanical force.^[22] This

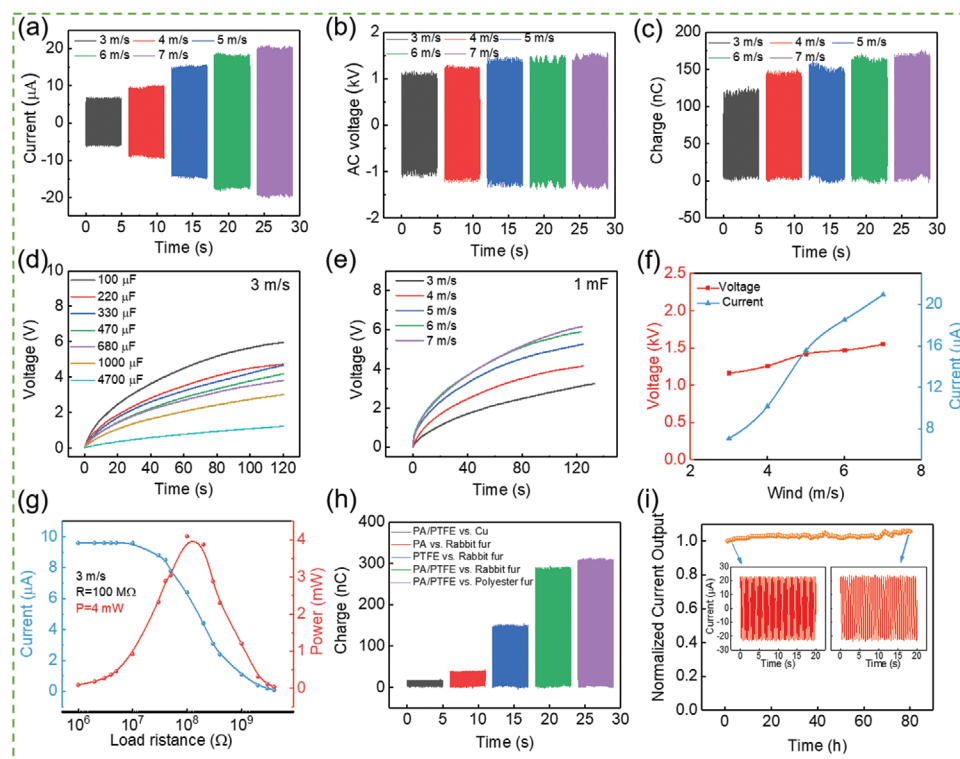


Figure 4. Characterization of output performance of a single AG-TENG assembly under fan conditions. a) short circuit current, b) open circuit voltage, c) amount of transferred charge at different wind speeds. d) The charging characteristic curves of capacitors with different capacities under the wind speed of 3 m s^{-1} . e) The charging characteristics of 1 mF capacitors at different wind speeds. f) The output change curve of current and voltage under different wind speeds. g) Peak power and average power curves under the condition of 3 m s^{-1} . h) Output effect chart of changing to different materials i) Durability test chart of the device.

technique is similar as electrostatic chucks (e-chucks) that play an important role in various wafer-processing equipment in the semiconductor industry.^[24] The rotor is tightly attached to the upper surface of the fan blade, and the fan blade drives the rotor to contact the stator when it rotates. Moreover, the structure designed in this way will reduce the device wear and performance degradation, ensuring the robustness and stability of the anti-glare device.

In addition, to realize the fast charging of AG-TENG, it is particularly important to use a matching energy management circuit (EM). Figure 5b shows the schematic diagram of the management circuit we used. The EM circuit uses a gas discharge tube (GDT) as a switch for energy accumulation and release, which can achieve the purpose of fast charging the capacitor.^[19a] As shown in Figure 5c, the charging speed is faster than before connecting to the circuit, it is increased by ≈ 10 times, and the 1 mF capacitor can be charged to 3 V in 20 s . Detailed parameters of the EM are in Note S2 (Supporting Information).

A series of application demonstrations were made under the condition of a wind speed of 5 m s^{-1} . Figure 5d and Video S1 (Supporting Information), show the device driving a wireless alarm within 40 s . In addition, the device can supply power to three commercial thermo-hygrometers at the same time, the storage capacitance is 1 mF , and it can work continuously and stably (Figure 5e; Video S2, Supporting information). Furthermore, to demonstrate its application potential for powering electrical devices on highways, we show in Figure 5f and

Video S3 (Supporting Information) that the AG-TENG can harvest wind energy through the circuit shown in Figure S6 (Supporting Information), as a set of red, yellow, and green traffic lights composed of LED arrays are powered (total power is 6 W). More importantly, as a wind energy harvester, AG-TENG can also power wireless Bluetooth devices, as shown in Figure 5g and Video S4 (Supporting Information), a commercial thermo-hygrometer with Bluetooth transmission function, driven by TENG. Under the application, the environmental information can be successfully transmitted to the mobile phone, and the temperature and humidity data can be displayed in real-time on the application interface through the temporary energy storage capacitor of 1 mF (Video S4, Supporting Information).

Furthermore, to demonstrate its powerful charging capability, we tried to drive 21 thermo-hygrometers. After charging the 10 mF capacitor for 4 min , it can drive 21 thermo-hygrometers to work at the same time for 20 s (Figure 5h). The entire running process is recorded in Video S5 (Supporting Information). Finally, under the same experimental conditions, 500 light-emitting diodes (LEDs) were also directly lit by the hybrid device (Figure 5i; Video S6, Supporting Information).

2.5. Application of AG-TENG Device on Highway

Based on the strong wind energy collection capability of AG-TENG, it can be used as a highway wind energy collection

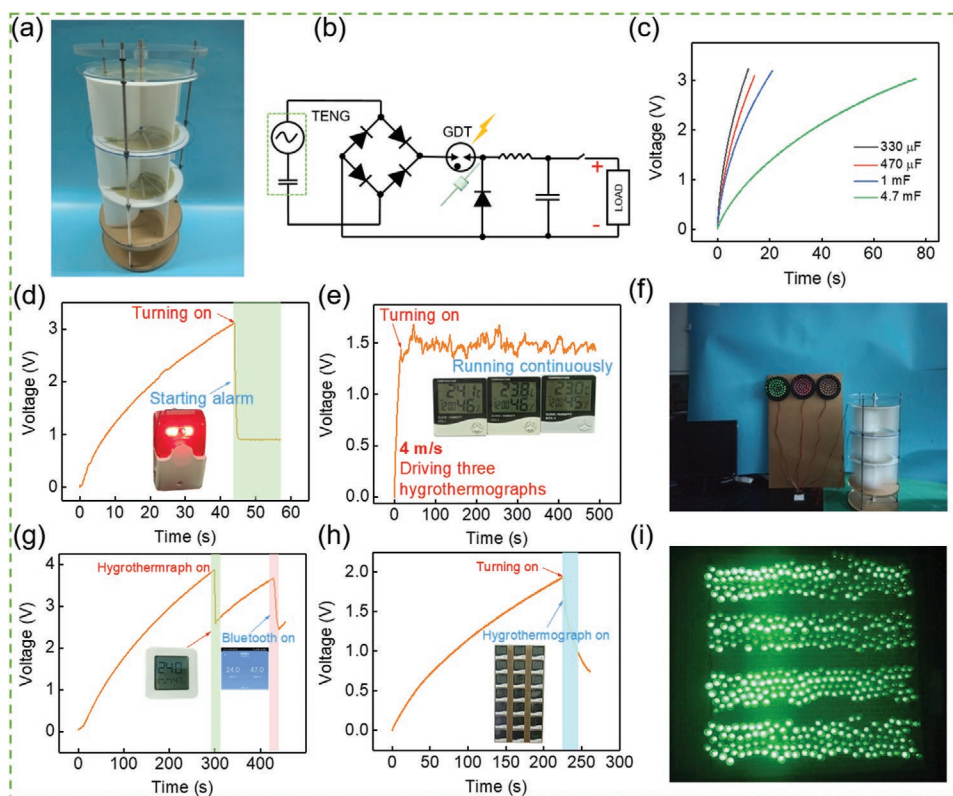


Figure 5. Application demonstration of the AG-TENG device. a) Photograph of the assembled AG-TENG. The materials and design of rotor and stator is mentioned in Experimental Section. b) Schematic diagram of the EM circuit. c) The charging characteristic curve of different capacitors after connecting the circuit. d) Driving the wireless alarm e) The charging voltage on the 1 mF capacitor when powering three hygrometers connected in parallel, driven by the AG-TENG at 5 ms⁻¹. f) Light up three traffic lights at the same time. g) Voltage distribution on a commercial hygrometer with bluetooth transmission, continuously powered by AG-TENG. h) Power supply for 21 commercial thermo-hygrometers at the same time, 4 min can make it work continuously for 20 s. i) 500 LEDs lighted up by the AG-TENG.

device, installed in the highway median. The AG-TENG has the following advantages: a) the design of the light-blocking structure makes it a candidate to replace the anti-glare board; b) The unique fan-blade structure reduces drag force on the panel; c) The modular tertiary structure design makes it easier to replace, ensuring the cost of application. **Figure 6a** shows the possibility of using this device for highway environmental monitoring. The anti-glare panel mainly blocks the light through the width and thickness of the panel, and at the same time scatters the light beam and reflects it, reducing the intensity of the light beam to prevent the glare of the headlamp of the opposite car. The overall width of the device is 22 cm, which is consistent with the width of commercial anti-glare boards. We show the anti-glare effect of AG-TENGs in **Figure 6b**, which meets the basic requirements of anti-glare panels: incoming light blocking, good lateral visibility, and little psychological impact on drivers. In addition, the current output and charging effect of one device (3 units) and two devices (6 units) in parallel under different wind speeds were tested respectively. As shown in **Figure S7** (Supporting Information), the output current is positively correlated with the number of array devices. The charging speed increases with the number of devices. This further confirms the idea that the array can be used on the highway.

To demonstrate its application potential on the highway, we developed a vehicle identification and recording system, consisting of an active RFID tag driven by AG-TENG and an RFID receiver powered by vehicles. As shown in **Figure 6c**, we simulated that when a vehicle passes an RFID tag driven by AG-TENG at the wind speed of 5 m s⁻¹, the card reader on the vehicle receives the wireless signal and records it. The RFID card can send electromagnetic wave signals and the receiver in the car can receive the signal in a long-range (≈20 m). The signal can work as a trigger for the receiver (easily powered by the car) to start recording. The receiver could potentially record the vehicle information such as receiving time, geographical location, travel path, and average car speed and upload the information to the cloud servers. However, we didn't focus on the receiver and give it that many function such as GPS and cloud uploading, although it can be achieved in the future. To demonstrate the feasibility of the integrated system, we experimentally tested the working time of the RFID system after a single charge. When the 680 uF capacitor is charged from 0 to 4.5 V, the switch is turned on. At this time, the RFID tag starts to transmit signals. The whole system will send signals to the card reader every 2 s, which will consume a small part of the electric energy. The RFID system continued to work for 13 min before shutting down (**Figure 6d**). The red light will flash when

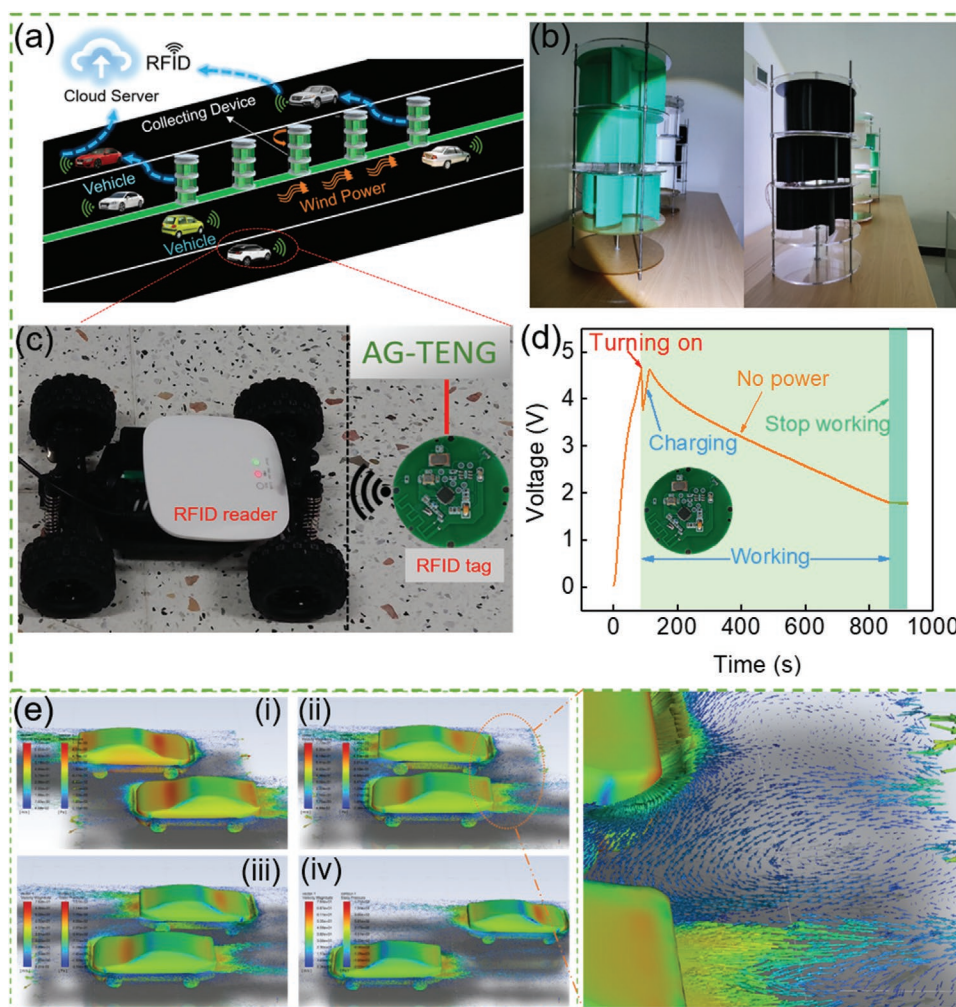


Figure 6. Application of AG-TENG on intelligent highways. a) Vehicle lane map of AG-TENG on highways. b) Anti-glare effect of AG-TENG under simulated high beam illumination. c) Photo of RFID card reader receiving signal. d) AG-TENG is used to drive commercial RFID systems to transmit signals. e) Simulation of the surrounding flow field change when the oncoming vehicle meets. The inset is an enlarged view of the flow field between the two cars when they meet.

signal is received and the whole process is recorded in Video S7 (Supporting Information). This provides a possible scheme for vehicle information monitoring on the highway.

In Figure 6e, ANSYS Fluent is used to simulate the change of flow field distribution around two vehicles when they meet. The illustration shows the change of the flow field between the wakes when the opposite vehicles met. It can be seen that the wind and vortices directions are conducive to the favorable rotation of the fan blades. In addition, we tested the operation of the AG-TENG unit on the road while the car was passing, and the result was that the unit started to operate when the car passed at a speed of 20 km h^{-1} . As shown in Figure S8 (Supporting Information), a photograph of a car passing by is shown at different viewing angles.

According to the experimental data, the average power generation of one AG-TENG unit (3 modules) is $\approx 0.095 \text{ kWh}$ per day under the minimum starting wind speed of 3 m s^{-1} . If 200 AG-TENG unit systems are installed on a 1 km long section, the roughly estimated power generation is $\approx 19 \text{ kWh}$ per day.

The above results show that the installation of AG-TENG along the central isolation belt of the highway can directly provide the power for the sensing device on the highway to work in a short time, which has great application potential in the intelligent highway system.

3. Conclusion

We developed a robust soft-contact TENG as anti-glare panels to harvest wind energy on highways. The TENG used ternary electrodes to maximize the output and force-balance spacing feature to reduce potential friction and wear. In fact, the average power density is 0.2 Wm^{-2} and the device shows no degradation after 1440000 cycles (80 h). After integrating the management circuit, the energy generated by simulated wind can charge and power low-consumption IoT devices on highways, such as signal lights and the RFID system for highway monitoring and identification. The features and proper design of the

system allow it to harvest highway wind energy on large scale with a minimum road hazard, making it a promising strategy for smarter and more efficient highways.

4. Experimental Section

Fabrication of AG-TENG: TENG device consists of a stator and a rotor. Stator: I) Used a laser cutting machine (PLS6.75) to cut an acrylic disc with an inner diameter of 16 mm and an outer diameter of 160 mm as a base; II) Used AD software to design a grid structure with an inner diameter of 16 mm and an outer diameter of 160 mm, and there are 12 grids on the upper surface of the stator. The copper electrode with a central angle of 30° and a thickness of 20 μm was printed on the FR-4 substrate with the designed copper grid electrode. The thickness of the substrate was 1.6 mm, a 4*65 mm slot was left between the grid, and the minimum gap between the edges of two adjacent electrodes was 4 mm. III) Used acrylic glue to attach the printed PCB grid panel to the cut acrylic substrate, stick double-sided tape (3 M LSE) in the cut grooves every three grooves, and finally put the cut polyester. The fur was glued to the cut slot where the tape was attached, as shown in Figure 3a. It is worth noting that the fur used in the laboratory, as a mature product, was easily available in the market at a lower price. Here, the polyester fur that could be mass-produced on the market was selected, the artificial wool was combined with the fabric, and it was obtained through a series of processing processes such as tanning. The weight of the processed fur was 0.74 kg m⁻¹, and the hair length was ≈2 cm. After trimming, it could be attached to the substrate as a part of the triboelectric material.

Rotor: I) An acrylic base panel (thickness: 1 mm) as a substrate was cut into a disk having an outer diameter of 160 mm and an inner diameter of 16 mm with a laser cutter. II) Used an acrylic substrate as the base, and then used a laser cutting machine to draw grid lines corresponding to the stator on the substrate. III) Attached PTFE film (50 μm in thickness) and nylon film (25 μm in thickness) alternately on the surface of the acrylic substrate, and cut along the groove with a knife, as shown in Figure 3a.

The polyester fibers were cut into long strips 65 mm long and 4 mm wide, which was optimal for the charge transfer and electrostatic induction surface area. The PTFE film and the Nylon film were alternately attached to the disk-shaped substrate with a 4 mm gap to form the rotor; the corresponding stator electrodes were also left with a 4 mm gap between them to match the rotor. The 4 mm gap gave enough space for the installation of polyester fibers to give enough transferred charges and did not reduce the electrostatic induction surface area between the stator and rotor significantly. Assembly of the AG-TENG Device: I) Used a laser cutting machine to cut two acrylic substrates with an inner diameter of 8 mm and an outer diameter of 225 mm as bases, and the substrate thickness was 5 mm. II) Drilled three small holes with a diameter of 5 mm on the edge of the substrate respectively, and inserted a fully threaded screw rod into the small hole to fix the base. The screw rod was made of 304 stainless steel, with an outer diameter of 5 mm and a length of 50 cm. III) Used an optical axis to penetrate the two substrates, and the optical axis was made of 304 stainless steel, with a diameter of 8 mm and a length of 50 cm. Fan blade: The designed fan blade adopted the Savonius type fan blade structure, with a width of 20 cm, a height of 10 cm, and a thickness of 2 mm. The whole was made of PETG material 3D printing, which not only ensured toughness but also has the characteristics of light, thin, and high-temperature resistance. IV) Finally, the fan blades, rotors, and stators were fixed on the optical axis in sequence, and three basic TENG units were installed in total. The three basic TENG units were connected in parallel and worked independently.

Electrical Measurement and Characterization: All equipment was fixed on an optical table for measurement. Rotational movement was performed using a rotary motor (60ST-MO1930). Short circuit current, transfer charge, and open circuit voltage were measured with an electrometer (Keithley 6517). The wind was generated by a commercial

fan (SE-A200), controlled by an AC governor (ZADY6000X, CHNK, China), and the wind speed was tested by a digital anemometer (AS856, SMART SENSOR, China).

Supporting Information

Supporting Information is available from the Wiley Online Library or from the author.

Acknowledgements

Support from the National Key R & D Project from Minister of Science and Technology (2021YFA1201601), National Natural Science Foundation of China (Grant No. 52192610) was appreciated. E.S. thanks Yaxing Cao and Zhenxing Ding for device fabrications and measurements.

Conflict of Interest

The authors declare no conflict of interest.

Data Availability Statement

The data that support the findings of this study are available from the corresponding author upon reasonable request.

Keywords

anti-glare panels, green energy, highway wind energy, TENG wind turbines

Received: December 22, 2022

Revised: January 16, 2023

Published online:

- [1] a) D. Yoo, S.-C. Park, S. Lee, J.-Y. Sim, I. Song, D. Choi, H. Lim, D. S. Kim, *Nano Energy* **2019**, 57, 424; b) P. Chen, J. An, R. Cheng, S. Shu, A. Berbille, T. Jiang, Z. L. Wang, *Energy Environ. Sci.* **2021**, 14, 4523; c) J. Han, Y. Feng, P. Chen, X. Liang, H. Pang, T. Jiang, Z. L. Wang, *Adv. Funct. Mater.* **2021**, 32, 2108580; d) Z. Zhou, X. Li, Y. Wu, H. Zhang, Z. Lin, K. Meng, Z. Lin, Q. He, C. Sun, J. Yang, Z. L. Wang, *Nano Energy* **2018**, 53, 501.
- [2] C. Lapointe, H. Gopalan, *J. Sol. Energy Eng.* **2016**, 138, 024503.
- [3] W. L. Tian, Z. Y. Mao, X. Y. An, B. S. Zhang, H. B. Wen, *Energy* **2017**, 141, 715.
- [4] M. Kumar, K. Kumar, *Technol. Lett.* **2016**, 3, 10.
- [5] S. S. Hegde, A. Thamban, S. P. M. Bhai, A. Ahmed, M. Upadhyay, A. Joishy, A. Mahalingam, *Proceedings of the ASME International Mechanical Engineering Congress and Exposition*, ASME, New York **2016**.
- [6] W. Y. Hu, E. Jiaqiang, Y. W. Deng, L. J. Li, D. D. Han, X. H. Zhao, Z. Q. Zhang, Q. G. Peng, *Energy Convers. Manage.* **2018**, 171, 249.
- [7] a) J. J. Han, Y. Liu, Y. W. Feng, T. Jiang, Z. L. Wang, *Adv. Energy Mater.* **2022**, 2203219; b) S. A. Basith, A. Chandrasekhar, *Nano Energy* **2023**, 108, 108183; c) C. Ye, D. Liu, P. Chen, L. N. Y. Cao, X. Li, T. Jiang, Z. L. Wang, *Adv. Mater.* **2022**, 2209713; d) H. Li, J. Wen, Z. Ou, E. Su, F. Xing, Y. Yang, Y. Sun, Z. L. Wang, B. Chen, *Adv. Funct. Mater.* **2023**, 2212207; e) G. Li, S. Fu, C. Luo, P. Wang,

- Y. Du, Y. Tang, Z. Wang, W. He, W. Liu, H. Guo, J. Chen, C. Hu, *Nano Energy* **2022**, 96, 107068.
- [8] a) H. Ryu, J. H. Lee, U. Khan, S. S. Kwak, R. Hinchet, S. W. Kim, *Energy Environ. Sci.* **2018**, 11, 2057; b) Y. Wang, E. Yang, T. Y. Chen, J. Y. Wang, Z. Y. Hu, J. C. Mi, X. X. Pan, M. Y. Xu, *Nano Energy* **2020**, 78, 105279; c) B. Dudem, N. D. Huynh, W. Kim, D. H. Kim, H. J. Hwang, D. Choi, J. S. Yu, *Nano Energy* **2017**, 42, 269.
- [9] a) Z. L. Wang, T. Jiang, L. Xu, *Nano Energy* **2017**, 39, 9; b) J. An, Z. M. Wang, T. Jiang, X. Liang, Z. L. Wang, *Adv. Funct. Mater.* **2019**, 29, 1904867; c) K. Q. Xia, J. M. Fu, Z. W. Xu, *Adv. Energy Mater.* **2020**, 10, 2000426.
- [10] a) R. Hinchet, H. J. Yoon, H. Ryu, M. K. Kim, E. K. Choi, D. S. Kim, S. W. Kim, *Science* **2019**, 365, 491; b) M. T. Rahman, S. M. S. Rana, M. Salauddin, P. Maharjan, T. Bhatta, J. Y. Park, *Adv. Energy Mater.* **2020**, 10, 1903663; c) A. R. Mule, B. Dudem, S. A. Graham, J. S. Yu, *Adv. Funct. Mater.* **2019**, 29, 1807779.
- [11] a) J. Nie, Z. Ren, L. Xu, S. Lin, F. Zhan, X. Chen, Z. L. Wang, *Adv. Mater.* **2020**, 32, 1905696; b) S. Y. Li, Y. Fan, H. Q. Chen, J. H. Nie, Y. X. Liang, X. L. Tao, J. Zhang, X. Y. Chen, E. G. Fu, Z. L. Wang, *Energy Environ. Sci.* **2020**, 13, 896.
- [12] a) F. R. Fan, Z. Q. Tian, Z. L. Wang, *Nano Energy* **2012**, 1, 328; b) C. Ye, K. Dong, J. An, J. Yi, X. Peng, C. Ning, Z. L. Wang, *ACS Energy Lett.* **2021**, 6, 1443; c) Z. L. Wang, J. Song, *Science* **2006**, 312, 242; d) Z. Ren, Z. Wang, Z. Liu, L. Wang, H. Guo, L. Li, S. Li, X. Chen, W. Tang, Z. L. Wang, *Adv. Energy Mater.* **2020**, 10, 2001770; e) P. Lu, H. Pang, J. Ren, Y. Feng, J. An, X. Liang, T. Jiang, Z. L. Wang, *Adv. Mater. Technol.* **2021**, 6, 2100496; f) A. Ahmed, I. Hassan, T. Ibn-Mohammed, H. Mostafa, I. M. Reaney, L. S. C. Koh, J. Zu, Z. L. Wang, *Energy Environ. Sci.* **2017**, 10, 653.
- [13] X. Xiao, X. Q. Zhang, S. Y. Wang, H. Ouyang, P. F. Chen, L. G. Song, H. C. Yuan, Y. L. Ji, P. H. Wang, Z. Li, M. Y. Xu, Z. L. Wang, *Adv. Energy Mater.* **2019**, 9, 1902460.
- [14] a) J. An, P. Chen, Z. Wang, A. Berbille, H. Pang, Y. Jiang, T. Jiang, Z. L. Wang, *Adv. Mater.* **2021**, 33, 2101891; b) Z. Sun, M. Zhu, X. Shan, C. Lee, *Nat. Commun.* **2022**, 13, 5224; c) D. Wei, F. Yang, Z. Jiang, Z. Wang, *Nat. Commun.* **2022**, 13, 4965; d) W. Liu, Y. Duo, J. Liu, F. Yuan, L. Li, L. Li, G. Wang, B. Chen, S. Wang, H. Yang, Y. Liu, Y. Mo, Y. Wang, B. Fang, F. Sun, X. Ding, C. Zhang, L. Wen, *Nat. Commun.* **2022**, 13, 5030; e) J. H. Zhang, Z. Li, J. Xu, J. Li, K. Yan, W. Cheng, M. Xin, T. Zhu, J. Du, S. Chen, X. An, Z. Zhou, L. Cheng, S. Ying, J. Zhang, X. Gao, Q. Zhang, X. Jia, Y. Shi, L. Pan, *Nat. Commun.* **2022**, 13, 5839.
- [15] Z. Wang, J. An, J. Nie, J. Luo, J. Shao, T. Jiang, B. Chen, W. Tang, Z. L. Wang, *Adv. Mater.* **2020**, 32, 2001466.
- [16] a) B. Zhang, J. Chen, L. Jin, W. Deng, L. Zhang, H. Zhang, M. Zhu, W. Yang, Z. L. Wang, *ACS Nano* **2016**, 10, 6241; b) L. N. Y. Cao, Z. Xu, Z. L. Wang, *Nanomaterials* **2022**, 12, 3261.
- [17] Y. X. Bian, T. Jiang, T. X. Xiao, W. P. Gong, X. Cao, Z. N. Wang, Z. L. Wang, *Adv. Mater. Technol.* **2018**, 3, 1700317.
- [18] C. G. Zhang, Y. B. Liu, B. F. Zhang, O. Yang, W. Yuan, L. X. He, X. L. Wei, J. Wang, Z. L. Wang, *ACS Energy Lett.* **2021**, 6, 1490.
- [19] a) Y. Liu, W. J. Yan, J. J. Han, B. D. Chen, Z. L. Wang, *Adv. Funct. Mater.* **2022**, 32, 2202964; b) Y. J. Luo, P. F. Chen, L. N. Y. Cao, Z. J. Xu, Y. Wu, G. F. He, T. Jiang, Z. L. Wang, *Adv. Funct. Mater.* **2022**, 32, 2205710.
- [20] T. Morbiato, C. Borri, R. Vitaliani, *Appl. Energy* **2014**, 133, 152.
- [21] Q. Li, W. Liu, H. Yang, W. He, L. Long, M. Wu, X. Zhang, Y. Xi, C. Hu, Z. L. Wang, *Nano Energy* **2021**, 90, 106585.
- [22] D. Liu, C. Y. Li, P. F. Chen, X. Zhao, W. Tang, Z. L. Wang, *Adv. Energy Mater.* **2022**, 13, 2202691.
- [23] a) Y. Fang, T. Tang, Y. Li, C. Hou, F. Wen, Z. Yang, T. Chen, L. Sun, H. Liu, C. Lee, *iScience* **2021**, 24, 102300; b) X. Fu, S. Xu, Y. Gao, X. Zhang, G. Liu, H. Zhou, Y. Lv, C. Zhang, Z. L. Wang, *ACS Energy Lett.* **2021**, 6, 2343; c) X. Li, Y. Cao, X. Yu, Y. Xu, Y. Yang, S. Liu, T. Cheng, Z. L. Wang, *Appl. Energy* **2022**, 306, 117977; d) S. Liu, X. Li, Y. Wang, Y. Yang, L. Meng, T. Cheng, Z. L. Wang, *Nano Energy* **2021**, 83, 105851; e) S. Yong, J. Wang, L. Yang, H. Wang, H. Luo, R. Liao, Z. L. Wang, *Adv. Energy Mater.* **2021**, 11, 2101194.
- [24] H. Imamura, K. Kadooka, M. Taya, *Soft Matter* **2017**, 13, 3440.